

Regulation of morphology and magnetic properties of $ZnFe_2O_4$ assemblies via magnetic fields

Xian Zhang(张贤), Jing Meng(孟静), Yeguo Sun(孙业国), Zhe Qu(屈哲), Jun Cao(曹俊), and Yongqing Ma(马永青)
Citation: Chin. Phys. B, 2026, 35 (**7**): 077509. DOI: 10.1088/1674-1056/ae5591
http://cpb.iphy.ac.cn; http://iopscience.iop.org/cpb

What follows is a list of articles you may be interested in

A design for an antiferromagnetic material based on self-assembly for information storage

Si-Yan Gao(高思妍), Yi-Feng Zheng(郑益峰), Shu-Qiang He(何述强), Haiping Fang(方海平), and Yue-Yu Zhang(张越宇)
Chin. Phys. B, 2025, 34 (**6**): 067504. DOI: 10.1088/1674-1056/adc6f5

Cu-doped nanocomposite $Pr_2Fe_{14}B/\alpha$-Fe ribbons with high $(BH)_{max}$

Mehran Khan Alam, Shahzab Raza, Chengyong Gao(高成勇), Guangbing Han(韩广兵), and Shishou Kang(康仕寿)
Chin. Phys. B, 2024, 33 (**12**): 127504. DOI: 10.1088/1674-1056/ad8cba

Impact of Co^{2+} substitution on structure and magnetic properties of M-type strontium ferrite with different Fe/Sr ratios

Yang Sun(孙洋), Ruoshui Liu(刘若水), Huayang Gong(宫华扬), and Baogen Shen(沈保根)
Chin. Phys. B, 2024, 33 (**10**): 107506. DOI: 10.1088/1674-1056/ad6554

Tuning magneto-dielectric properties of Co_2Z ferrites via Gd doping for high-frequency applications

Jian Wu(武剑), Bing Lu(卢冰), Ying Zhang(张颖), Yixin Chen(陈一鑫), Kai Sun(孙凯), Daming Chen(陈大明), Qiang Li(李强), Yingli Liu(刘颖力), and Jie Li(李颉)
Chin. Phys. B, 2023, 32 (**9**): 097501. DOI: 10.1088/1674-1056/acc3f7

Control of the interparticle spacing in superparamagnetic iron oxide nanoparticle clusters by surface ligand engineering

Dan Wang(王丹), Bingbing Lin(林兵兵), Taipeng Shen(申太鹏), Jun Wu(吴君), Fuhua Hao(豪富华), Chunchao Xia(夏春潮), Qiyong Gong(龚启勇), Huiru Tang(唐惠儒), Bin Song(宋彬), Hua Ai(艾华)
Chin. Phys. B, 2016, 25 (**7**): 077504. DOI: 10.1088/1674-1056/25/7/077504

Regulation of morphology and magnetic properties of $ZnFe_2O_4$ assemblies via magnetic fields

Xian Zhang(张贤)[1,4,5,†], Jing Meng(孟静)[3], Yeguo Sun(孙业国)[1], Zhe Qu(屈哲)[4], Jun Cao(曹俊)[5], and Yongqing Ma(马永青)[2]

[1] *Anhui Province Key Laboratory of Low-Temperature Co-Fired Materials, School of Electronic Engineering, Huainan Normal University, Huainan* 232038, *China*

[2] *Engineering Technology Research Center of Magnetic Materials, School of Physics and Materials Science, Anhui University, Hefei* 230039, *China*

[3] *School of Economics and Management, Huainan Normal University, Huainan* 232038, *China*

[4] *Anhui Key Laboratory of Low-Energy Quantum Materials and Devices, High Magnetic Field Laboratory, HFIPS, Chinese Academy of Sciences, Hefei* 230031 *China*

[5] *Anhui Saifu Electronics Limited Company, Tongling* 244000, *China*

(Received 27 October 2025; revised manuscript received 19 March 2026; accepted manuscript online 23 March 2026)

$ZnFe_2O_4$ was synthesized at 200 °C via a solvothermal pathway using acetylacetonate salts of zinc and iron as raw materials in self-developed magnetic fields of varying intensities. The following phenomena were observed. During the synthesis process, applying a magnetic field causes spherical assemblies with micrometer-scale diameters to transform into coarse chain-like aggregates exhibiting a length-to-diameter ratio of approximately 4.8. As the strength of the magnetic field increases, the $ZnFe_2O_4$ particle size gradually decreases. The synthetic magnetic field causes the magnetization value of $ZnFe_2O_4$ to increase or decrease. This is due to the interaction between surface spins and bulk spins, and this interaction is regulated by the particle size. The zero-field-cooling (ZFC) curves measured under a 100-Oe (1 Oe = 79.5775 $A{\cdot}m^{-1}$) magnetic field obey the Curie–Weiss law in the high-temperature region. The effective magnetic moments of the superparamagnetic particles obtained through fitting are $\mu_{sp} = 2.53 \times 10^4\ \mu_B$ ($ZnFe_2O_4$ prepared under the condition without magnetic field), $\mu_{sp} = 1.69 \times 10^4\ \mu_B$ ($ZnFe_2O_4$ prepared under the condition of two magnets), and $\mu_{sp} = 1.85 \times 10^4\ \mu_B$ ($ZnFe_2O_4$ prepared under the condition of four magnets). The estimated magnetic particle sizes are 11.4 nm, 10.6 nm, and 9.9 nm, respectively, which are larger than the corresponding sizes (8.6 nm, 7.2 nm, and 6.2 nm) obtained from electron microscopy, indicating that the magnetic moments of adjacent particles tend to be parallel. This work reports a new approach that enables the preparation of magnetic particles with clean surfaces as well as tunable sizes, morphologies, and properties simply by adjusting the magnetic field strength without the need for any additives or templates, thus broadening their potential for various applications.

Keywords: assembly, magnetic-field-assisted synthesis, morphology, magnetic properties

PACS: 75.50.Gg, 75.75.–c

DOI: 10.1088/1674-1056/ae5591 **CSTR:** 32038.14.CPB.ae5591

1. Introduction

The ordered nanostructures of magnetic materials have attracted considerable attention due to their potential applications in high-density data storage, magnetic resonance imaging, medical diagnosis, targeted drug delivery, *etc*.[1,2] Reported synthesis methods for nano-assembly systems include the template method,[3,4] as well as approaches assisted by alternating electric fields[5] and surfactants.[6] Template-assisted synthesis is usually adopted to prepare ordered magnetic nanostructures.[7] However, this preparation method is complex, may introduce impurities, and often increases production costs, which is not suitable for large-scale industrial applications. By contrast, the magnetic field-induced assembly method is a simple and feasible approach that can also provide clean surfaces.[8] Therefore, magnetic field-assisted synthesis is attracting the interest of the scientific community as a new simple and inexpensive method for preparing ordered nanostructure materials.

During the sample preparation process, the applied magnetic field reduces the surface energy and enhances the dipole–dipole interaction, thereby promoting crystal growth along the direction of the easy magnetization axis. In principle, when an external field is applied during liquid-phase synthesis, the nucleation rate (I) can be expressed as

$$I = I_0 \exp\left(\frac{-Q}{RT}\right) \exp\left(\frac{-\Delta G_c + \Delta G_H}{RT}\right).$$

Here, I is a constant, Q is the activation energy, R is Avogadro constant, T is the absolute temperature, ΔG_c is the Gibbs free energy, and $\Delta G_H = -\mu_0 \Delta M(T) H - \frac{1}{2}\Delta\chi H^2$ is the free energy change induced by the magnetic field, where μ is the vacuum permeability, ΔM and $\Delta\chi$ are the changes in magnetization intensity and susceptibility, respectively, and H is the strength of the applied magnetic field.[9–11] Therefore, an external magnetic field can alter crystal nucleation and growth. However,

[†]Corresponding author. E-mail: zhangxian035@163.com

© 2026 Chinese Physical Society and IOP Publishing Ltd. All rights, including for text and data mining, AI training, and similar technologies, are reserved.

the actual process may be much more complex as the solvent properties (such as density, viscosity, and boiling point), solute concentration, magnetic field distribution, and even the synthesis system structure all influence the morphology and properties of the assembly. Therefore, magnetic-field-assisted synthesis remains a constantly evolving research field.

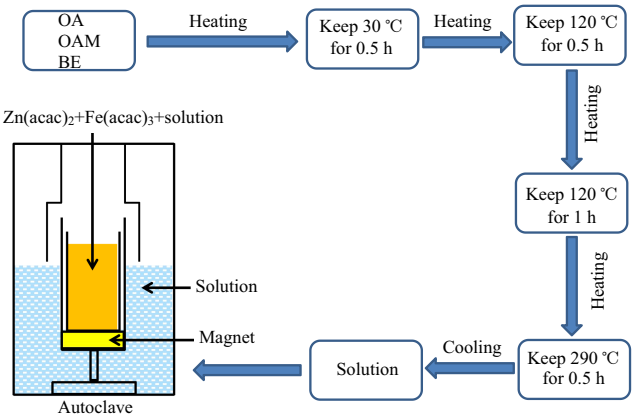
In this work, high-boiling-point solvents, namely oleic acid (OA), oleamine (OAM), and dibenzyl ether (BE), were selected, and acetylacetone salt was used as the raw material. The precursor solution was treated and then placed in a reaction vessel under varying magnetic field intensities to synthesize the $ZnFe_2O_4$ nanoparticle assemblies. The synthesized samples exhibit novel morphological features and magnetic properties.

2. Experimental procedures

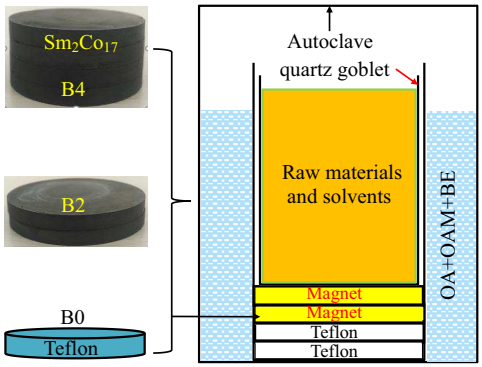
2.1. Synthesis of $ZnFe_2O_4$

OA (Aladdin, 85%), OAM (80%–90%), and BE (95%) were placed in a three-necked flask in a ratio of 1:1:4. The solution was magnetically stirred at 30 °C for 0.5 h to obtain an even mixture. It was then heated to 120 °C and held at this temperature for 30 min to remove any water or alcohol that might be present in the solution. It was protected with high-purity N_2 and heated to 200 °C for 1 hour. Finally, it was heated to 290 °C and held at this temperature for 30 min. After cooling to room temperature, the solution was used as a solvent for $ZnFe_2O_4$ synthesis. The preparation process is shown in Scheme 1.

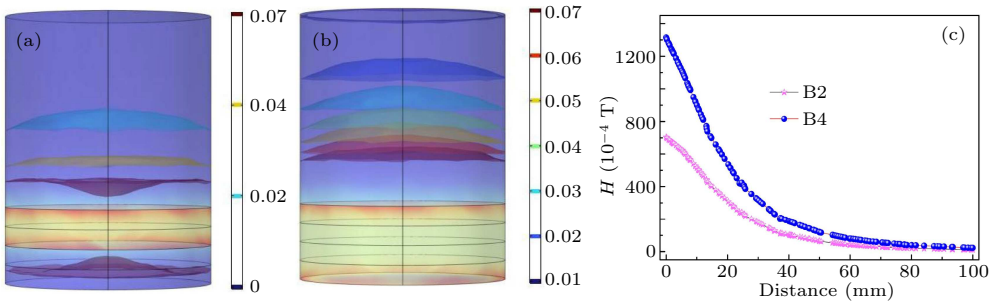
The reaction was carried out in a 1000-ml Hastelloy alloy autoclave (Parr 4500, USA). $Fe(acac)_3$ and $Zn(acac)_2$ were used as raw materials, mixed with the solvent, and placed in a quartz cup on a 50-mm-diameter circular Sm_2Co_{17} magnet. To minimize the influence of stray fields from the magnet edges, a matched configuration was employed between the sample holder and the magnet: the quartz cup (5 cm in diameter) was designed to match the diameter of the Sm_2Co_{17} circular magnet, and its center was aligned precisely with the magnet center. Based on the symmetry of the magnetic field distribution, this arrangement ensures that the magnetic field inside the quartz cup, where the sample is placed, is predominantly axial in direction. The magnetic field strength was changed by using different numbers of magnets (0, 2, and 4, denoted as B0, B2, and B4, respectively), as shown in Scheme 2. The $ZnFe_2O_4$ sample synthesized without applying any magnetic field (B0) is named Zn0, while the samples synthesized under the application of B2 and B4 magnets are named Zn2 and Zn4, respectively.



Scheme 1. Schematic diagram of the $ZnFe_2O_4$ synthesis process.



Scheme 2. Schematic diagram of the reaction vessel.



Scheme 3. Theoretical calculation and simulation results of magnetic field distribution. Among them, panel (a) is the three-dimensional magnetic field distribution simulation diagram above the B2 magnet, panel (b) is the corresponding magnetic field distribution of the B4 magnet, and panel (c) is the theoretical curve of magnetic field intensity varying with distance.

The COMSOL Multiphysics software was used to conduct a numerical simulation of the magnetic field distribution in the sample area of the Sm_2Co_{17} circular magnet and quartz cup used in the experiment. The results are shown in Scheme 3. Schemes 3(a) and 3(b) indicate that the magnetic field intensity at the same height of the reaction liquid surface has a small difference, and the magnetic field in the sample area is mainly in the axial component, and the stray field at the edge is negligible.

Based on the simulation results, the theoretical curve of the magnetic field variation with distance was obtained (Scheme 3(c)), and the experimental values were measured using the Hall magnetometer system (Table 1). The consistency of the theoretical and experimental results indicates that the magnetic field intensity gradually decreases with the increase of the distance from the magnet surface, showing a gradient feature of being near-strong and far-weak. It was found that the theoretical values were generally higher than the measured values. The main reason is that the magnet was in a high-temperature environment of 200 °C during the experiment, resulting in weakened magnetism and thus lower measurement results.

Table 1. Distribution of magnetic field with the distance from the surface of the magnet (experimental values).

Number of magnets \ Distance (cm)	0	1	2	3	4	5	6	8	9	10
B1 (10^{-4} T)	500	350	225	100	50	30	20	10	8	5
B2 (10^{-4} T)	620	400	220	130	80	50	35	16	12	10
B3 (10^{-4} T)	1000	600	360	220	140	90	60	30	20	15
B4 (10^{-4} T)	1200	800	450	250	150	100	64	32	24	20

A total of 400 mL of the OA/OAM/BE mixture (ratio of 1:1:4) was poured into the reaction vessel and used as the heat-transfer medium. The reaction setup is shown in Scheme 2. The reaction vessel was heated to 200 °C and kept at that temperature for 6 h; the precipitated substances were washed several times with alcohol and then dried to obtain the $ZnFe_2O_4$ samples.

2.2. Characterization

The crystal structure of the samples was characterized via x-ray diffraction (XRD, SmartLab 9KW, Rigaku Industrial Corporation, Osaka, Japan) with Cu-$K\alpha$ radiation (λ = 0.15406 nm). The chemical bonds of the samples were identified via Fourier-transform infrared spectroscopy (FTIR, Vertex80/Hyperion 2000, China). The morphology of the samples was analyzed using ultra-high-resolution scanning electron microscopy (SEM, REGULUS8230). The lattice fringes of the samples and the selected-area electron diffraction (SAED) images were acquired via high-resolution transmission electron microscopy (HRTEM, JEM-2100, Tokyo, Japan). The elemental composition, chemical state, and percentages of the samples were analyzed via x-ray photoelectron spectroscopy (XPS, Escalab 250Xi, Thermo, USA). The magnetic properties of the samples were investigated using a superconducting quantum interference device (MPMS3, Quantum Design, USA). Firstly, the samples were cooled in zero field, and then the zero-field-cooled (ZFC) magnetization curves were recorded upon increasing the temperature from 10 K to 390 K under a 100-Oe magnetic field. Subsequently, the samples were cooled again under a 100-Oe external magnetic field, and the field-cooled (FC) magnetization curves were acquired upon increasing the temperature from 10 K to 390 K.

3. Results and discussion

3.1. Analysis of the $ZnFe_2O_4$ crystal structure

Figure 1(a) shows the XRD pattern of the Zn0 sample and the standard PDF card of $ZnFe_2O_4$ (No. 22–1012). It can be observed that the Zn0 sample is a single-phase spinel structure with the Fd-3m (227) space group.[12] The lattice parameters a of the Zn0, Zn2, and Zn4 samples calculated using the expression $\sin^2\theta = \lambda^2(H^2+K^2+L^2)/4a^2$ are 8.4358 Å, 8.4357 Å, and 8.4358 Å, respectively; the x-ray densities dx calculated as d$x = ZM/N_a a^3$[13,14] are all 5.33 g/cm^3. Figure 1(b) shows the magnified XRD patterns (open circles) and corresponding Gaussian fitting curves (solid lines) near the strongest diffraction peaks for the three samples. The results indicate that the diffraction peak positions of the $ZnFe_2O_4$ synthesized under a magnetic field are not changed. This is different from the $CoFe_2O_4$ synthesized under a magnetic field, where peak shift occurs with increasing magnetic field strength.[15]

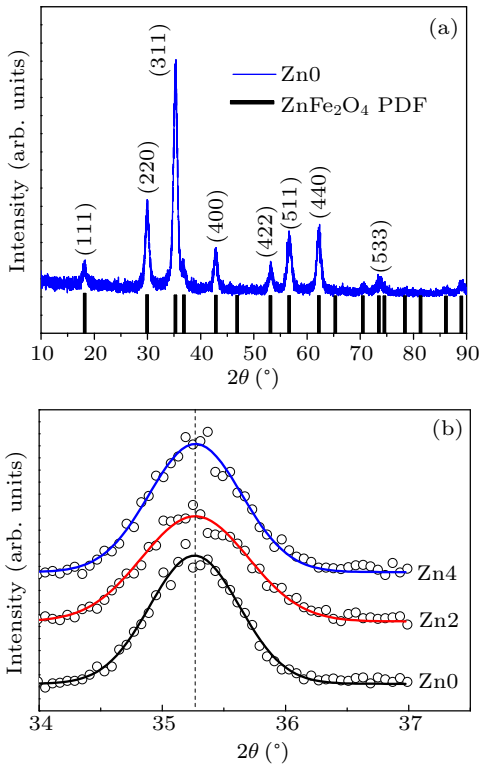


Fig. 1. The XRD pattern of Zn0 sample and standard PDF card of $ZnFe_2O_4$ (a). Magnified view of the XRD patterns around $2\theta = 35.26°$ for Zn0, Zn2, and Zn4 samples (b), where the solid lines are the fitted curves based on the Gaussian function.

$ZnFe_2O_4$ has a relatively low magnetic crystal anisotropy constant ($K_1 \approx 10^3$ J/m^3), which is much lower than that of

$CoFe_2O_4$ ($K_1 \approx 2 \times 10^5$ J/m^3). Under the influence of a magnetic field, the magnetoelastic effect can cause the shift of diffraction peaks through lattice strain, but its degree of influence is closely related to the magnetic crystal anisotropy: the larger the K_1 value, the more significant the regulation effect of the magnetic field on the lattice, and the more obvious the changes in lattice parameters and the corresponding peak position shifts. Due to the relatively weak magnetic crystal anisotropy of $ZnFe_2O_4$, no significant shift in the diffraction peak position was observed in the experiment.[16,17]

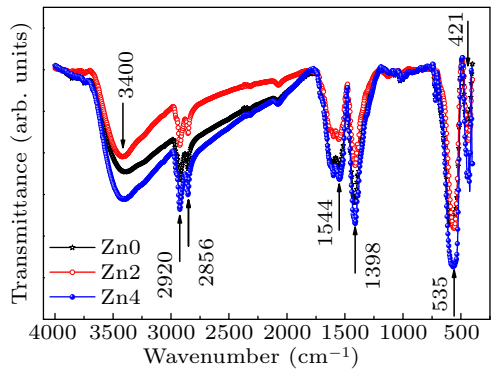


Fig. 2. FTIR spectra of Zn0, Zn2, and Zn4 samples.

The FTIR spectra of $ZnFe_2O_4$ exhibit absorption bands characteristic of the spinel ferrite structure (Fig. 2). The broad absorption band near 3400 cm^{-1} corresponds to the O–H stretching vibration of the hydroxyl groups adsorbed on the surface of nanoparticles. The absorption peaks at 2920 cm^{-1} and 2856 cm^{-1} are attributed to the C–H stretching vibration.[18] The absorption peaks at 1544 cm^{-1} and 1398 cm^{-1} are attributed to the O–H bending vibration, indicating the presence of adsorbed water on the nanoparticle surface.[19] The absorption peaks at 535 cm^{-1} and 421 cm^{-1} correspond to the stretching vibrations of the metal–oxygen bonds at the tetrahedral A sites and octahedral B sites, respectively.[20–22]

3.2. Analysis of the morphology and formation mechanism of $ZnFe_2O_4$

Figure 3 presents the SEM panels (a), (d), (g), TEM panels (b), (e), (h), and HRTEM panels (c), (f), (i) images of the Zn0, Zn2, and Zn4 samples. From Fig. 3(a), it can be seen that the Zn0 sample synthesized without any applied magnetic field comprises spherical-like particles and peanut-shaped particles of varying sizes (maximum diameter of approximately 3.0 μm) formed by the self-assembly of several spherical particles. The TEM image in Fig. 3(b) shows that the aggregates in the Zn0 sample are composed of particles with a size of approximately 8.6 nm. The lattice stripes with spacings of 0.48 nm and 0.24 nm observed in Figs. 3(c) and 3(i) correspond to (111) and (222) crystal planes of $ZnFe_2O_4$, respectively. The lattice stripes with a spacing of 0.12 nm observed in Fig. 3(f) correspond to (444) crystal planes of $ZnFe_2O_4$.

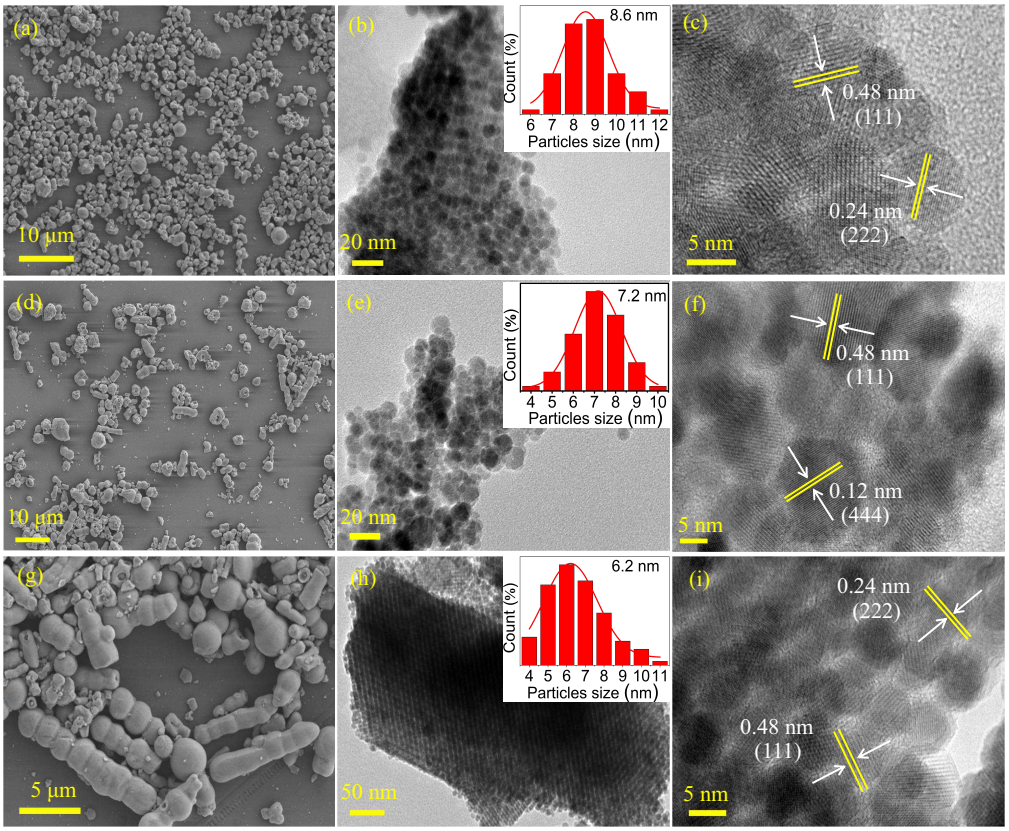


Fig. 3. SEM panels (a), (d), (g), TEM panels (b), (e), (h), and HRTEM panels (c), (f), (i) images of Zn0, Zn2, and Zn4 samples. The insets show the corresponding particle size distributions, where solid lines represent the Gaussian fitting curves.

From Fig. 3, it can be seen that the Zn2 and Zn4 samples synthesized under the external magnetic field display coarse chain-like structures composed of linked spherical particles. The coarse chain-like structures in the Zn4 sample are more distinct than those in the Zn2 sample. In the Zn4 sample, the coarse chain-like structures have varying lengths, with the maximum length being approximately 13.0 μm and the width being approximately 2.7 μm (aspect ratio of approximately 4.8). This aspect ratio is smaller than that of $CoFe_2O_4$ due to the weaker magnetism of $ZnFe_2O_4$ at the synthesis temperature (200 °C). At this temperature, the $ZnFe_2O_4$ particles cannot easily align along the magnetic field lines.[15] The coarse chain-like structures observed in $ZnFe_2O_4$ synthesized under magnetic field are clearly formed from the assembly of spherical particles: This is different from the rod-like assembled structures of $CoFe_2O_4$ under a magnetic field.[15] The synthesis was carried out at 200 °C. The Curie temperature of $CoFe_2O_4$ is 820 K,[23] so this material is still weakly ferromagnetic at 200 °C (473 K). On the other hand, $ZnFe_2O_4$ has become diamagnetic at 200 °C and thus has a very small magnetization. Due to the weaker magnetism of $ZnFe_2O_4$ with respect to $CoFe_2O_4$, the nanoparticles of nano-sized $ZnFe_2O_4$ are subjected to a smaller magnetic force and struggle to align along the magnetic field lines; however, as the nanoparticles aggregate into larger spherical particles, the magnetism is enhanced, and they are assembled into coarse chains under the action of the magnetic force. This process is depicted in Figs. 4(b)–4(d).

From Fig. 3, it can be seen that the particle sizes of the Zn2 and Zn4 samples are 7.2 nm and 6.2 nm, respectively, both smaller than the particle size of the Zn0 sample. This indicates that under magnetic-field-assisted synthesis, the particles become smaller, which is consistent with previous results on $CoFe_2O_4$ synthesized under magnetic field.[15] Liang *et al.* used a magnetic field to assist the hydrothermal synthesis of $CoFe_2O_4$[24] and also observed the formation of smaller particles when a magnetic field was applied during synthesis, which is due to the fact that the magnetic field increases the nucleation rate of $CoFe_2O_4$. This is because the expression for the grain size is $d = \sqrt[4]{v/I}$, where I is the nucleation rate, and v is the grain growth rate;[25,26] thus, an increase in nucleation rate results in a reduced grain size.

The mechanism by which the magnetic field affects the nucleation rate can be summarized as two aspects. On one hand, the thermodynamic mechanism (reducing the nucleation energy barrier): As shown in the formula in the introduction, the applied magnetic field reduces the total nucleation energy barrier by introducing the magnetic free energy term ΔG_{H}. For paramagnetic or weakly magnetic precursor ion clusters or initial crystal nuclei, they will be magnetized in the magnetic field, and their magnetic moments tend to align along the magnetic field direction. This ordering reduces the entropy of the system, thereby reducing the Gibbs free energy change (ΔG_{c}) required to form the critical crystal nucleus. The reduction of the nucleation energy barrier directly leads to an exponential increase in the nucleation rate I.

On the other hand, the kinetic mechanism (facilitating ion migration and collisions) is as follows: In a solvothermal environment, the dissolved Fe^{3+} and Zn^{2+} ions and their complexes have certain effective magnetic moments. The gradient magnetic field will exert a magnetic force on these moving ions, which can be superimposed on the thermal motion (diffusion) of the ions, directing the ions to migrate towards the high magnetic field region (*i.e.*, near the magnet surface).[24] This magnetically induced migration increases the local supersaturation, thereby enhancing the probability of effective collisions between ions, and the formation of stable nuclei. The studies by An *et al.* on $CoFe_2O_4$[24] and by Jin *et al.* on IN100 alloys[26] support this view. They attribute the grain refinement under the magnetic field to the increase in the nucleation rate. Our recent study on $CoFe_2O_4$[15] also observed the same phenomenon, further supporting the universality of this mechanism.

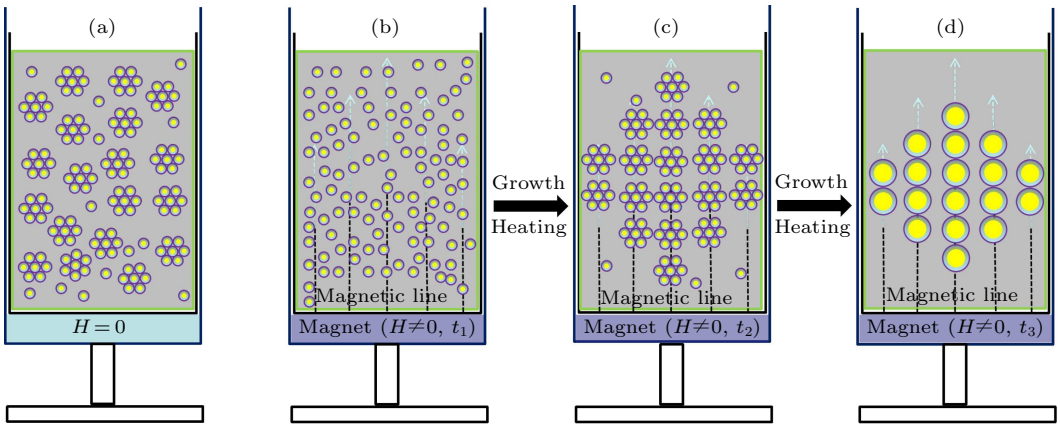


Fig. 4. Schematic diagram of the formation mechanism of $ZnFe_2O_4$: (a) $H = 0$; (b) $He0, t_1$; (c) $He0, t_2$ ($t_2 > t_1$); (d) $He0, t_3$ ($t_3 > t_2$).

3.3. Analysis of the oxidation state of $ZnFe_2O_4$

Figure 5 presents the core-level XPS spectra for Zn 2p, Fe 2p, and O 1s in Zn0, Zn2, and Zn4 samples.[27,28] The fitting curves are also shown, and the fitting results are listed in Table 2. The fitting results indicate that all Zn^{2+} ions in $ZnFe_2O_4$ occupy the tetrahedral sites. During the synthesis process, the application of a magnetic field causes irregular changes in the proportion of Fe ions in the tetrahedral and octahedral sites, as well as fluctuations in the chemical state proportions of the O ions.

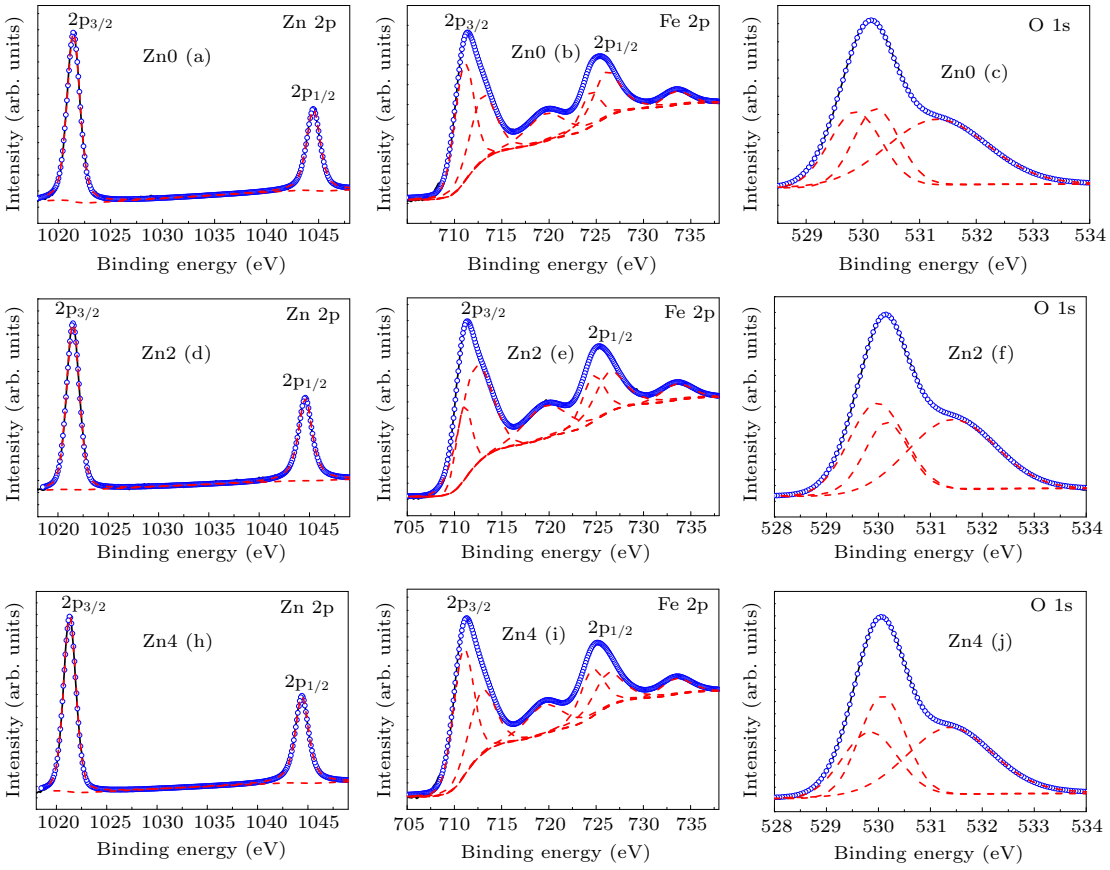


Fig. 5. Core level XPS spectra for Zn 2p, Fe 2p, and O 1s in Zn0, Zn2, and Zn4 samples. The solid lines denote the experimental data, the dashes lines represent the fitting curves, and the empty circles are the sum of the fitting curves.

Table 2. Binding energy (BE) and area percentage of the XPS peaks for Zn, Fe, and O in the Zn0, Zn2, and Zn4 samples.

$ZnFe_2O_4$	Contribution	Zn0			Zn2			Zn4		
		BE (eV)	% Area		BE (eV)	% Area		BE (eV)	% Area	
Zn	Td	1021.4	65		1021.5	62		1021.3	62	
		1044.4	35		1044.5	38		1044.4	38	
Fe	Oh	711.0	29	38	710.9	13	25	710.9	30	45
		724.4	9		724.6	12		724.5	15	
	Td	712.9	23	43	712.2	36	54	712.9	21	35
		726.0	20		726.3	18		726.2	14	
	Sat	719.6	15	19	719.5	15	21	719.4	15	20
		733.4	4		733.4	6		733.4	5	
O	/	529.8	27		529.9	35		529.8	25	
	/	530.2	26		530.1	23		530.0	32	
	/	531.3	47		531.4	42		531.3	43	

3.4. Analysis of magnetic properties of $ZnFe_2O_4$

Figure 6 shows the magnetization–magnetic field (M–H) loops of the Zn0, Zn2, and Zn4 samples at 2 K and 300 K. Their characteristics are similar to those previously reported for $ZnFe_2O_4$, and the magnetization values are also similar.[29] For comparison, $ZnFe_2O_4$ bulk materials synthesized via the co-precipitation method and calcined at 600 °C exhibit clear magnetic hysteresis at 10 K, with a coercivity of 165 Oe and a saturation magnetization of 28 emu/g. At 300 K, these bulk samples do not show any magnetic hysteresis but rather exhibit superparamagnetic behavior, with a saturation magnetization of only 4 emu/g.[30]

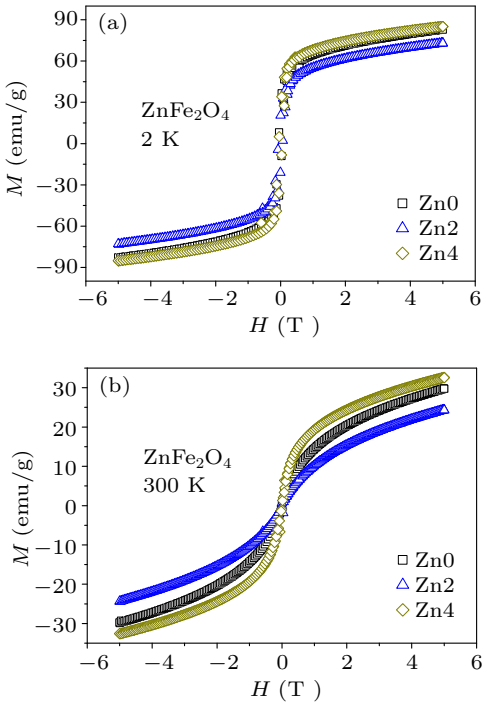


Fig. 6. M–H loops (-5 T $< H <$ 5 T) measured at 2 K (a) and 300 K (b) of the Zn0, Zn2, and Zn4 samples.

At 2 K, the particle magnetic moment is in an obstructive state (see Fig. 7). All three samples exhibit significant magnetic hysteresis, showing typical ferromagnetic behavior. At higher magnetic fields, the magnetization and demagnetization curves almost overlap, and the M–H relationship becomes almost linear. At the maximum applied magnetic field ($H = 5$ T), the magnetization reaches the maximum value, here denoted as M_{max}, but it does not reach saturation. This paramagnetic contribution mainly originates from two types of tilted spins.[29] (i) Tilted spins within the particles: The molecular field within $ZnFe_2O_4$ particles is very weak, so the coupling with the external field is also very weak. Therefore, the magnetic moments within the particles are tilted. (ii) Tilted magnetic moments on the particle surface: At 300 K, the hysteresis loop is hardly observed, and the magnetization intensity is still very large, which is indicative of superparamagnetic behavior. Table 3 lists the magnetic parameters extracted from the above loops, including H_c, M_{max}, M_r, and M_r/M_{max}.

As shown in Table 3, the applied magnetic field during synthesis leads to either an increase or a decrease in the magnetization of $ZnFe_2O_4$, which can be attributed to the competing effects between surface spin disorder and particle size variation. The disorder of surface spin is a typical characteristic of nanomagnetic particles, and its degree of disorder is closely related to the particle size.[31] For $ZnFe_2O_4$ nanoparticles, the small size effect will lead to insufficient coordination number of surface atoms, preventing the formation of an ordered arrangement of surface spin consistent with the bulk phase, resulting in spin tilting or disordered layers.[32] The applied gradient magnetic field acts on the particle magnetic moment through the magnetic force, and on the one hand, it promotes the directional arrangement of the particle assembly, and on the other hand, it regulates the disordered state of the surface spin.[15] When the magnetic field strength is relatively small, the polarization effect of the magnetic field on the surface spin is weak, and the influence of the disordered surface spin layer dominates, resulting in a lower magnetization intensity; as the magnetic field strength increases, the polarization effect of the magnetic field on the surface spin strengthens, causing some disordered surface spins to tend to form an ordered arrangement, while the particle size decreases due to the increase in nucleation rate (the proportion of surface spin further increases), and the competition between these two factors leads to a non-monotonic change in magnetization intensity.[33]

Table 3. H_c, M_{max}, M_r, and M_r/M_{max} at 2 K and 300 K for the Zn0, Zn2, and Zn4 samples.

$ZnFe_2O_4$	2 K				300 K			
	H_c (Oe)	M_{max} (emu/g)	M_r (emu/g)	M_r/M_{max}	H_c (Oe)	M_{max} (emu/g)	M_r (emu/g)	M_r/M_{max}
Zn0	562	82.9	22.2	0.27	76	29.7	0.4	0.012
Zn2	648	73.3	21.4	0.29	426	24.3	0.6	0.025
Zn4	524	85.1	19.8	0.23	48	32.6	0.3	0.009

Figure 7 shows the temperature dependence of the FC and ZFC magnetization ($M(T)$ curves) of the three samples (Zn0, Zn2, and Zn4) under a 100-Oe (a)–(c) and a 3-T (d) magnetic field. The temperatures corresponding to the maximum values of the ZFC curves measured at 100 Oe, namely the blocking temperatures (T_B), are 47, 26, and 60 K, respectively. Below T_B, both the FC and ZFC magnetizations decrease with decreasing temperature because the magnetic moments of the particles are gradually frozen in their respective anisotropy axes, and magnetic moment switching is hindered. This results in a superparamagnetic glass-like state. Above T_B, thermal fluctuations (k_BT) promote a disordered arrangement of the particle magnetic moments, leading to a monotonic decrease in magnetization down to zero, which is characteristic of superparamagnetic behavior. As shown in Fig. 7(d), the FC and ZFC curves measured under a 3-T magnetic field overlap. In the low-temperature region, the magnetization decreases with decreasing temperature, indicating that even this stronger magnetic field is insufficient to realign the magnetic moments in the direction of the magnetic field within the glass state.

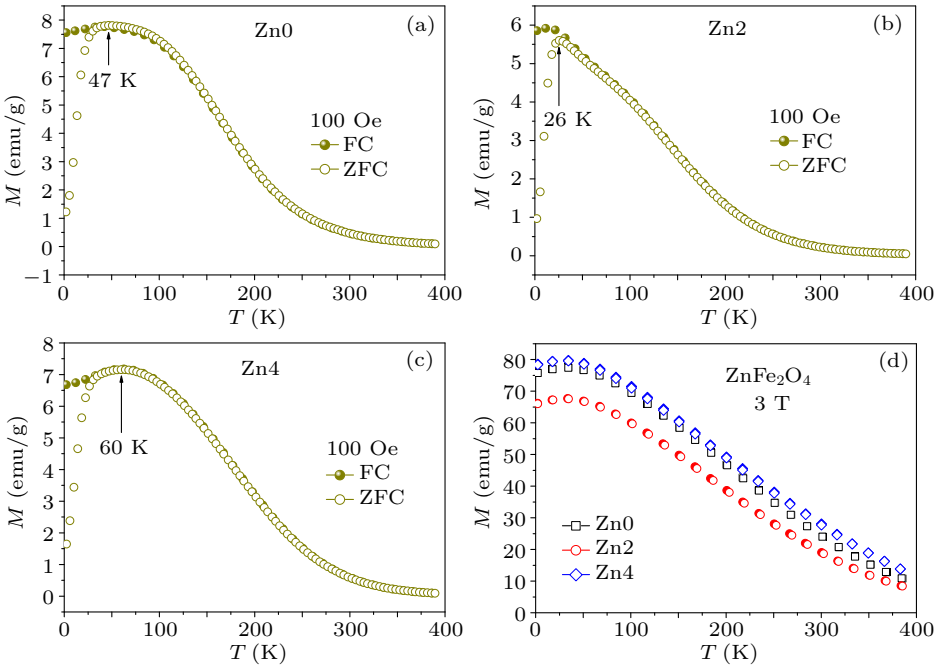


Fig. 7. FC and ZFC magnetization (M) curves as a function of temperature (T) measured at $H = 100$ Oe (a)–(d) and $H = 3$ T (f) for the Zn0, Zn2, and Zn4 samples.

Above 360 K, the ZFC curve can be fitted using Bloch's law $M(T) = M_0\left[1 - BT^{3/2}\right]$,[27,34,35] where M_0 is the magnetization at 0 K and B is a constant. The fitting results, shown in Fig. 8, yield M_0 values of 43, 33, and 51 emu/g, respectively.

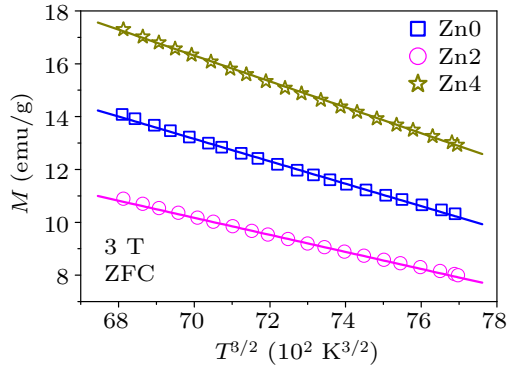


Fig. 8. Experimental (empty symbols) and fitted data (solid lines) using Bloch's law under 3 T at a temperature above 360 K for the Zn0, Zn2, and Zn4 samples.

The ZFC curves of the Zn0, Zn2, and Zn4 samples measured at 100 Oe can be fitted using Curie's law $\chi(T) = \frac{C}{T - T_{CW}}$ within a certain temperature range.[29] Here, C is the Curie constant, and T_{CW} is the Curie temperature. The fitting results for the Zn0, Zn2, and Zn4 samples yield C and T_{CW} values of 16.9 $cm^3 \cdot K \cdot mol^{-1}$ and 317 K, 9.2 $cm^3 \cdot K \cdot mol^{-1}$ and 312 K, and 13.5 $cm^3 \cdot K \cdot mol^{-1}$ and 328 K, respectively.

According to Refs. [29,36,37], the effective superparamagnetic magnetic moment μ_{sp} of the Zn0, Zn2, and Zn4 samples (which represents the average magnetic moment of the superparamagnetic particles) was estimated from the slope of the fitting curves in Fig. 9. Here, M_s is the saturation magnetization at 300 K. Taking the Zn0 sample as an example, the effective superparamagnetic magnetic moment μ_{sp} is calculated as follows:[15]

$$\mu_{sp} = \frac{3k_B}{M_s\,\mu_B}\frac{1}{\text{Slope}} = \frac{3 \times 1.3805 \times 10^{-16}\ (\text{erg/K})}{29.7\ (\text{emu/g}) \times 0.927 \times 10^{-20}\ (\text{erg/Oe})} \times \frac{1}{0.05934}\left(\frac{\text{emu}\cdot\text{K}}{\text{g}\cdot\text{Oe}}\right) = 2.53 \times 10^4\ \mu_B.$$

At 300 K, the maximum magnetization of Zn0 is 29.7 emu/g (1.28 μ_B/f.u.). A crystal cell of $CoFe_2O_4$ contains eight molecular formulas, and the unit-cell volume (a^3) of $ZnFe_2O_4$ is 601 $Å^3$. Therefore, the size of the magnetic particles (R) of the Zn0 sample can be calculated according to the following expression:

$$R = \sqrt[3]{\frac{\mu_{sp}}{\mu_B/\text{f.u.} \times 8} \times a^3} = \sqrt[3]{\frac{2.53 \times 10^4}{1.28 \times 8} \times 601} = 11.4\ \text{nm}.$$

The calculated values of the effective superparamagnetic magnetic moment μ_{sp} of the Zn0, Zn2, and Zn4 samples are $2.53 \times 10^4\ \mu_B$, $1.69 \times 10^4\ \mu_B$, and $1.85 \times 10^4\ \mu_B$, respectively. The corresponding maximum magnetization values at 300 K are 29.7 emu/g (1.28 μ_B/f.u.), 24.3 emu/g (1.05 μ_B/f.u.), and 32.6 emu/g (1.41 μ_B/f.u.), respectively. The magnetic particle sizes (R) of the Zn0, Zn2, and Zn4 samples are estimated to be 11.4 nm, 10.6 nm, and 9.9 nm, respectively, which are larger than the particle sizes obtained from the TEM results (8.6 nm, 7.2 nm, and 6.2 nm). A possible reason for this discrepancy is that within the investigated temperature range, the magnetic

particles may not be completely in a pure superparamagnetic state.[37] Thus, the magnetic moments of neighboring particles may become parallel due to the interaction between neighboring particles, resulting in an increase in the overall magnetic ordering degree.

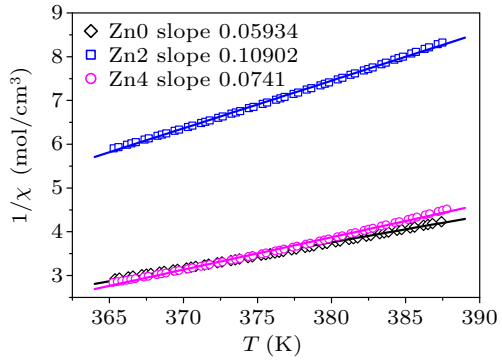


Fig. 9. Temperature dependence of the ZFC inverse magnetic susceptibility: experimental data (empty symbols) and fitted curves (solid lines) obtained from the Curie–Weiss law for the Zn0, Zn2, and Zn4 samples.

4. Conclusions

In this study, $ZnFe_2O_4$ nano-assemblies were synthesized by the magnetic field-assisted solvothermal method. It was found that the magnetic field could induce the transformation of the micrometer spherical assemblies into a coarse chain-like structure with a length-to-diameter ratio of approximately 4.8. As the magnetic field strength increased (from B0 to B4), the particle size decreased from 8.6 nm to 6.2 nm, which was attributed to the increase in the nucleation rate due to the magnetic field. The analysis of magnetic properties indicated that the effective superparamagnetic moments were 2.53×10^4 μ_B (for Zn0), 1.69×10^4 μ_B (for Zn2), and 1.85×10^4 μ_B (for Zn4). The change in magnetization intensity was influenced by the competition between surface spins and particle size. Based on the fitting of Curie–Weiss law, the magnetic order sizes (11.4 nm, 10.6 nm, 9.9 nm) obtained were larger than the TEM observation values, indicating that the magnetic moments of adjacent particles tended to be parallelly arranged. This work provides a clean and controllable synthesis pathway for regulating the morphology and magnetic properties of $ZnFe_2O_4$ without the need for templates through magnetic field manipulation.

Acknowledgements

Project supported by the Key Projects of the Natural Science Research of the Higher Education Institutions of Anhui Province, China (Grant No. 2025AHGXZK31120) and the Provincial Quality Engineering Project of the Higher Education Institutions of Anhui Province, China (Grant No. 2023zybj047).

References

[1] Majetich S A and Sachan M 2006 *J. Phys. D: Appl. Phys.* **39** R407
[2] Cowburn R P and Welland M E 2000 *Science* **287** 1466
[3] Folkard A L, Anyanwu V O and Friedrich H B 2025 *J. Porous Mater.* **32** 1443
[4] Antonel P S, Oliveira C L P, Jorge G A, Perez O E, Leyva A G and Negri R M 2015 *J. Nanopart Res.* **17** 294
[5] Alotaibi S, Samba J, Pokharel S, Lan Y C, Uradu K, Afolabi A, Unlu I, Basnet G, Aslan K, Flanders B N, Lisfi A and Ozturk B 2018 *Appl. Phys. Lett.* **112** 092401
[6] Zhou L, Fu Q Y, Zhou D X, Zheng Z P, Hu Y X, Luo W, Tian Y T, Wang C H, Xue F and Tang X H 2017 *Appl. Phys. Lett.* **111** 032903
[7] Lu H B, Liao L, Li J C, Shuai M and Liu Y L 2008 *Appl. Phys. Lett.* **92** 093102
[8] Sun X and Ma Y Q 2018 *Ceram. Int.* **44** 23305
[9] Wang J H, Ma Y W and Watanabe K 2008 *Chem. Mater.* **20** 20
[10] Kumar P and Kumar R 2015 *Thin Solid Films* **592** 155
[11] Zhang C, Mo Z, Guo R B, Teng G X and Zhao G P 2014 *Mater. Res. Bull.* **53** 116
[12] Dong Y C, Xia Y, Chui Y S, Cao C W and Zapien J A 2015 *J. Power Sources* **275** 769
[13] Zhao B B and Nan Z D 2012 *J. Mater. Chem.* **22** 6581
[14] Hashim M, Koo B H, Shirsath S E, Mohamme E M, Shah J, Kotnala R K, Choi H K, Chung H and Kumar R 2012 *J. Alloys Compd.* **518** 11
[15] Zhang X, Kan X C, Wang M, Rao R, Zheng G H, Wang M L and Ma Y Q 2021 *J. Cryst. Growth* **565** 126131
[16] Benitez M J, Petracic O, Tüysüz H, Schüth F and Zabel H 2011 *Phys. Rev. B* **83** 134424
[17] Oliver S A 2000 *J. Appl. Phys.* **87** 5633
[18] Moradi L and Mahdipour P 2019 *Appl. Organometal. Chem.* **33** e4996
[19] Giri A, Makhal A, Ghosh B, Raychaudhuri A K and Pal S K 2010 *Nanoscale* **2** 2704
[20] Nasir M F M, Salehmin M N I, Mamat M H, Kassim M B, Alrokayan S A H, Khan H A, Hussain T and Mahmood M R 2025 *J. Mater. Sci: Mater. Electron.* **36** 362
[21] Kumari H, Chahal S, Singh R M, Kumar A and Parmar R 2025 *J. Electron. Mater.* **54** 6454
[22] Saafan S A, El?Nimr M K, Hussein M M and Omar M K 2021 *Appl. Phys. A* **127** 800
[23] Franco A and Silva F C 2010 *Appl. Phys. Lett.* **96** 172505
[24] Ma K, Wang Z, Tao T X, Xu S, Rehman S, Yan X, Fang J, Chen R G, Wang H, Zhang X, Xie C, Lu Y, Lu Q R and Wang J F 2022 *ACS Appl. Nano Mater.* **5** 7410
[25] Yao B, Ding B Z, Sui G L, Wang A M and Hu Z Q 1996 *J. Mater. Res.* **11** 912
[26] Jin W Z, Bai F D, Li T J and Yin G M 2008 *Mater. Lett.* **62** 1585
[27] Qiao Y, Xiao J P, Jia Q, Lu L Y and Fan H L 2019 *Results Phys.* **13** 102221
[28] Behera A, Mansingh S, Das K K and Parida K 2019 *J. Colloid Interface Sci.* **544** 96
[29] Veronica B G and Regino S P 2012 *J. Mater. Chem.* **22** 2992
[30] Dey S, Mondal R, Majumder S, Dasgupta P, Poddar A, Banerjee S and Kumar S 2018 *Mater. Today Proc.* **5** 9855
[31] Blanco G V, Saez P R and Torralvo F M J 2012 *J. Mater. Chem.* **22** 2992
[32] Skoropata E, Su T T and Ouyang H 2017 *Phys. Rev. B* **96** 024447
[33] Ojha V H and Kant K M 2019 *Physica B* **567** 87
[34] Vitta S, Khuntia A, Ravikumar G and Bahadur D 2008 *J. Magn. Magn. Mater.* **320** 182
[35] Skoropata E, Su T T, Ouyang H, Freeland J W and Lierop J V 2017 *Phys. Rev. B* **96** 024447
[36] Veronica B G, Adrian A C, Javier S B, Esteban U G, Regino S P and María J T F 2019 *J. Chem. Phys. C* **123** 16973
[37] Sun X, Ma Y Q, Xu S T, Xu Y F and Geng B Q 2015 *Mater. Charact.* **107** 34